



## Developing Geometric Analysis Tools to Compare Heat Map Results for Metal Additive Manufactured Components

R. Jill Urbanic<sup>1</sup> , Bitra Mohajernia<sup>2</sup>  and Navid Nazemi<sup>3</sup> 

<sup>1</sup>University of Windsor, [jurbanic@uwindsor.ca](mailto:jurbanic@uwindsor.ca)

<sup>2</sup>University of Windsor, [mohajerb@uwindsor.ca](mailto:mohajerb@uwindsor.ca)

<sup>3</sup>AECOM, [Navid.Nazemi@aecom.com](mailto:Navid.Nazemi@aecom.com)

Corresponding author: R. Jill Urbanic, [jurbanic@uwindsor.ca](mailto:jurbanic@uwindsor.ca)

**Abstract.** Developing predictive and optimization models for metal-based additive manufacturing (AM) processes to link part geometry, process parameters, build geometry and the resulting mechanical and physical properties is challenging. There are unique, rapid heat cycling characteristics with AM processes that influence the hardness, strength, and residual stress characteristics, which is the focus of this research. The component's properties are influenced by the tool path as well as the process settings. Developing a predictive model is complicated, as single bead observations are different from multiple bead configurations, and occurrences and magnitudes of the tensile and compressive stresses vary throughout the specimen. Therefore, approaches to extract information from heat maps resulting from calibrated finite element simulation models are explored. Images are converted into 2D and 3D geometry, and point cloud data generated to provide positional and residual stress data in a format that can be utilized for comparative and predictive modelling. Initial comparative and artificial neural network prediction models indicate the potential of these approaches.

**Keywords:** Metal Additive Manufacturing, Finite Element Modeling Geometric Based Interpretation, Physical Properties, Residual Stress, Comparative methods

**DOI:** <https://doi.org/10.14733/cadaps.2020.288-311>

### 1 INTRODUCTION

Laser cladding is usually utilized for coating surfaces to improve the performance of the surface (corrosion or wear resistance) or to repair it if it is worn. This process has evolved into a viable metal additive manufacturing (AM) solution for fabricating localized features onto an existing component, or to create a near net shape. Laser cladding is termed as direct energy deposition (DED) when being employed as an AM process. In this process, a laser beam melts the material powder flowing from a nozzle while it is being distributed onto a surface. A thin layer on the surface of the substrate melts to help forming a bond between the clad material and the substrate material. A shielding gas such as argon protects the melt pool from the atmosphere to prevent oxidization.

The DED input parameters play a significant role in the quality of the bead [4, 6, 9], the dilution zone (the region where the substrate and deposition materials mix), and the heat affected zone (HAZ) (shown in Fig. 1), as well as the bead geometry [1, 3, 7]. As a result, understanding the influence of the input parameters on the resulting mechanical and physical properties is a concern for both equipment manufacturers, and process planners or fabricators.

Each process input parameter (laser power, travel speed, powder feed rate, contact tip to work piece distance) has a distinct effect on the bead's mechanical and physical properties. For multiple beads (a more realistic scenario), the percentage overlap and the travel path (one way, zigzag, raster scan versus a contour-based solution, etc.) are also influences. It is crucial to find the best combination of input and operation parameters to deposit a bead with the desired geometry and mechanical properties. The generation of residual stresses due to the high thermal gradients, and the non-uniform plastic deformation of the base substrate or plate, are two of the most important issues when analyzing the mechanical properties of the bead. Residual stresses can lead to undesirable distortion and cracks; therefore, (i) understanding the residual stress characteristics, (ii) linking them to the bead geometry and input parameters, and (iii) developing predictive models are active areas of research. Item (i) is addressed by conducting experimentally calibrated finite element analyses to provide insights; however, items (ii) and (iii) have significant research challenges, as the induced residual stresses (or hardness) are not discrete values such as the bead geometry shape characteristics.

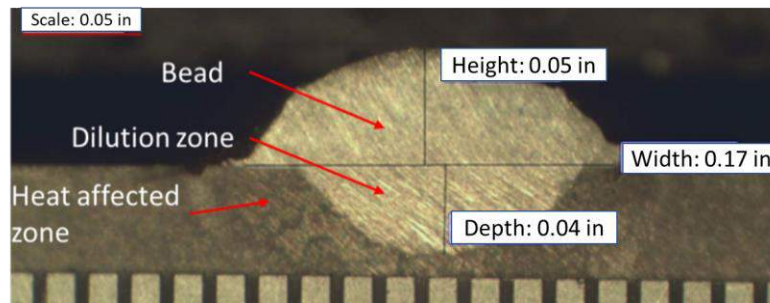


**Figure 1:** A single laser clad bead, showing the dilution and heat affected zones (with 0.2 mm gradients).

Prior AM DED research has been conducted utilizing P420 stainless steel as the clad material and AISI 1018 steel as the substrate material and a 4kW diode laser-robotic cell configuration. The bead length is 100 mm. The process parameters, factor levels for the design of experiments, and their corresponding values are presented in Table 1. The bead geometry for two experiments, labelled A and B, and their residual stress levels in the bead center, are illustrated in Fig. 2.

Parameters	Factor levels				
	-2	-1	0	1	2
Powder feed rate (gr/min)	10	<b>15</b>	<b>20</b>	25	30
Laser power (kW)	1	<b>2</b>	<b>2.5</b>	3	4
Focal length of lens (mm)	380	<b>390</b>	<b>400</b>	410	420
Laser speed (mm/s)	5	<b>7.5</b>	<b>10</b>	12.5	15
Contact tip to work piece distance (mm)	<b>21</b>	22	23	<b>24</b>	25

**Table 1:** Single bead experimental configuration, with the bolded text highlighting the process parameters for experiment A, and the red italicized text highlighting the process parameters for experiment B.

The residual stress measurement was conducted using the Proto X-ray diffraction system (Lab 002/LXRD 06024) [12] for two samples in the 'as clad' and 'heat treated' states. The operating parameters for the measurements are presented in Table 2. The samples were extracted from the center of the bead specimens. Six subsurface measurements were done – 0 represents the top of the bead. The upper and lower bounds (red dashed lines) are calculated from the collected data using a 90% confidence interval and used as a basis to assess the goodness of the developed finite element model.

The developed FEA model (using SYSWELD [17]) and the experimental results are presented for the non-heat treated (NHT) results in Fig. 2. The top of the bead is the 0 position, and the depth measurement is into the bead to the substrate. At the top of the bead, there is significant tensile stress, but it reduces as the bead depth increases. Slightly above the junction between the bead and the substrate, compressive stresses are observed. In the dilution zone, there are only compressive stresses. The observed inflection points are at the junction of the dilution and heat affected zones, and the HAZ and substrate. The FEA results correlate well to the experimental data. For a complete description of the model and mesh development, validation, experimental configuration and results, please refer to Nazemi and Urbanic [10].

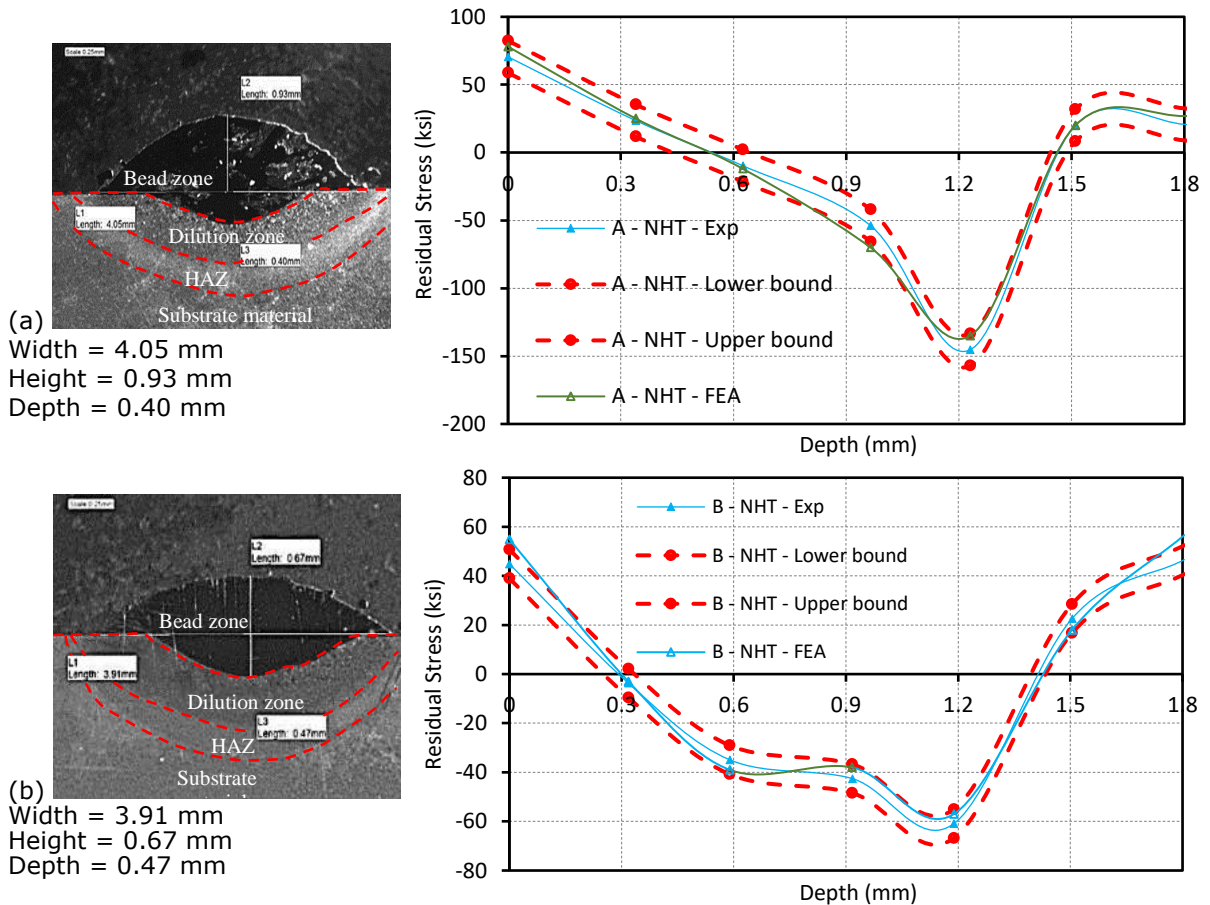


**Figure 2:** A single laser clad bead, showing the dilution and heat affected zones.

The results from the complete simulation model can be analyzed in regions of interest (Fig. 3). There are stress variations along the bead due to the heat flow and transient start-stop conditions (Fig. 3 (a)). It can be seen that the stress patterns are symmetric around the center axis (Fig. 3(b)).

Extending the model to analyze multiple beads with differing overlap and process configurations has been done [9, 10, 20]; however, the research question focuses on how to comprehensively compare results quantitatively and develop a predictive model that will encompass both the bead geometry and physical properties. The induced residual stress (and hardness, etc.) magnitudes and patterns will vary based on the input parameters and the bead overlap percentage. The goal of this research is to transform the mechanical or physical property heat maps, or isoline representations, for process build configurations into geometric data, which in turn can be used for comparison purposes and to seed an artificial neural network or other AI based predictive model.

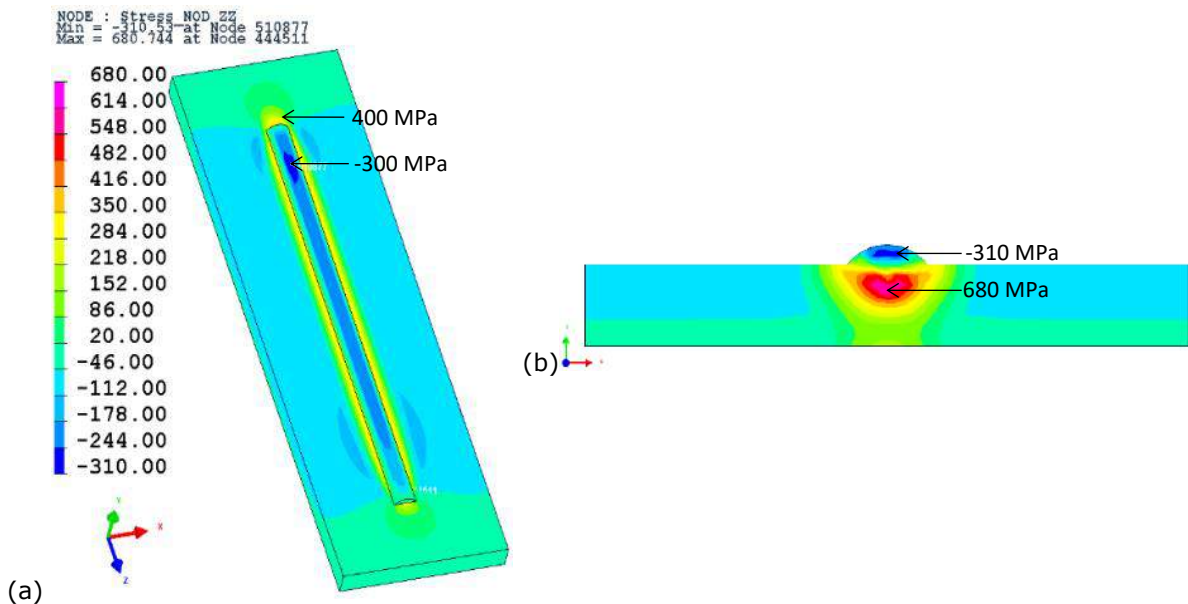


**Figure 3:** (a) Longitudinal residual stress contours for specimen A from the simulation (b) cross-section view (specimen center).

## 2 LITERATURE REVIEW

The connection between the processing parameters and the process's thermal history is a critical research topic for metal-based AM. Experimental studies are time consuming, and may be expensive, if residual stress and advanced microstructure analyses are performed. The use of analytical models is difficult, based on the fact that the metal bead-based deposition process is a highly complex non-linear problem that couples the multi-phase fluid phenomena, heat transfer, and metallurgical transformations. Consequently, numerical simulation is a powerful tool for analyzing AM to evaluate process parameter sets, and to predict desirable cladding results. Researchers have developed mass transfer [22], melt pool [8], and heat transfer models, which have been validated with physical experimental data. Several researchers have explored the influence of input parameters on the melt pool, bead geometry, hardness, and residual stresses - typically for one deposited bead. A selection of research papers is summarized in Table 2. In most of these studies metallurgical effects were ignored and simplifications and assumptions have been made to model the heat source and boundary conditions. The discussion typically focuses on a targeted comparison of the experimental and simulation results, or the influence of the simplifications. No comprehensive, quantitative

methodologies to compare properties or results and have been presented over a wide range of conditions or build scenarios.

Although predictive models have been developed for the bead geometry [1, 3, 15, 16], transient start-stop conditions [14], cornering, and the impact of the bead overlap percentages, travel path strategy, etc. all need to be considered when determining an optimal process plan strategy.

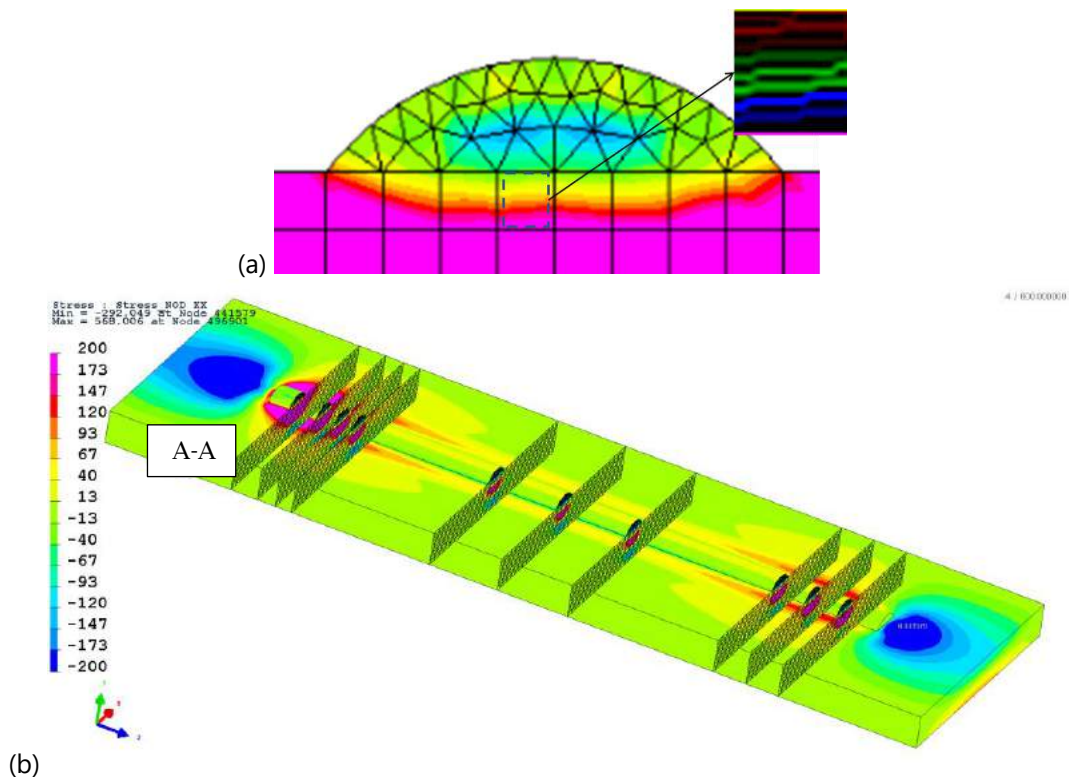
Author	No. of beads	Heat source	FEA (method)	Material
Aggarwal et al. (2018) [1]	1 and 3 beads	Laser (Gaussian), Experimental & statistical analyses		P420 stainless steel on AISI 1918
Balu et al. (2013) [2]	1 & 2 beads	Gaussian moving	3D thermo- mechanical	Ni-WC composite material, NT-60 over NT-20
Fallah et al. (2011) [5]	1 bead	Gaussian energy	Mass and heat transfer	AISI 304L Ti45Nb on Ti-6Al-4V.
Nazemi & Urbanic (2018) [9]	Multi beads	3D conical Gaussian moving	Thermo- mechanical- metallurgical modeling	P420 stainless steel on AISI 1918
Nazemi et al. (2017) [10]	Multi beads	3D conical Gaussian moving	Thermo- mechanical- metallurgical modeling	P420 stainless steel on AISI 1918
Palumbo et al. (2004) [11]	1 bead, and the melt pool shape	Gaussian energy	3D thermo- mechanical	Cu-based alloy
Song et al. (2014) [16]	Multi bead wall	Experimental & statistical analyses		2Cr13 stainless steel
Toyserkani et al. (2004) [18]	1 bead	Gaussian distribution	3-D transient FEA	Iron deposited onto mild steel
Toyserkani et al. (2003) [19]	1		Mass and heat transfer	P20 tool steel
Urbanic et al. (2018) [20]	Multiple beads – surface (Hybrid Manufacturing)	3D conical Gaussian moving	Thermo- mechanical- metallurgical modeling	420 stainless steel on Cold rolled structural steel

**Table 2:** Selected research publications related to metal AM bead geometry, simulations, and materials.

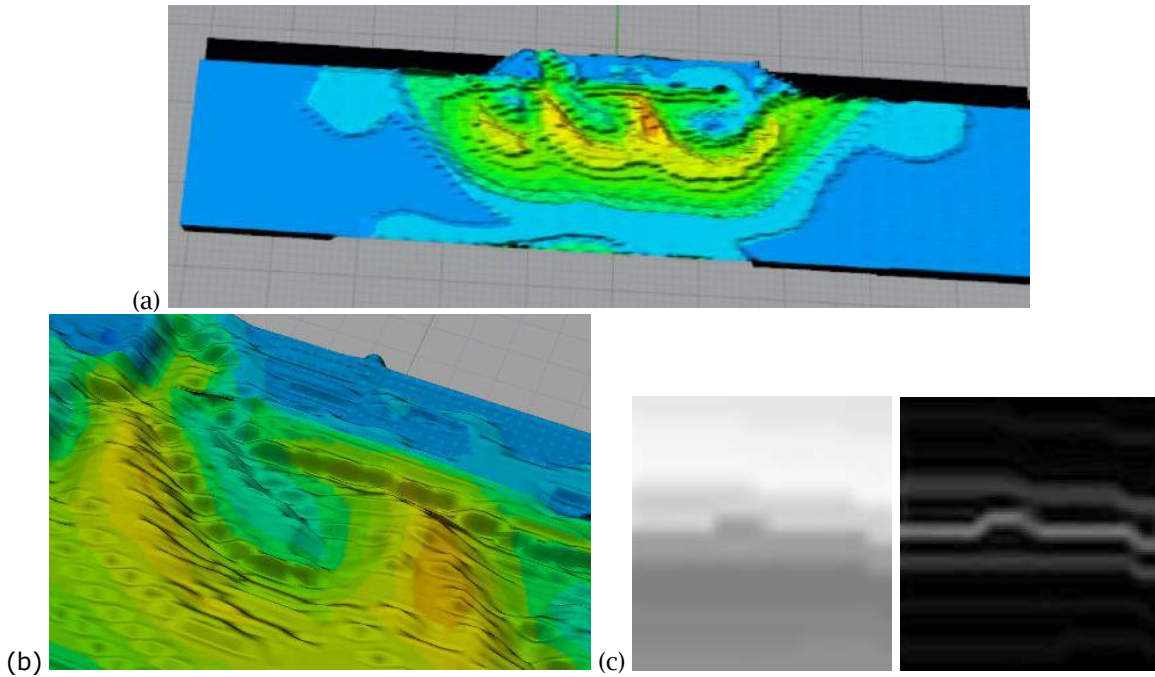
There are issues with granularity and scope to be considered. Most researchers present data on thermal histories and localized analyses in steady-state regions. An effective optimization model provides a systematic and quantitative way to evaluate and select decisions. Here, it should consider multiple criteria: the bead geometry, mechanical and physical properties at multiple points within the bead and the substrate, process settings, the tool path motions, and the transient and steady-state conditions. It should be flexible and extensible (i.e., not limited to one bead), and various process conditions and results should be captured. These are significant challenges to be addressed. Data fusion between experimental and simulation data should serve as a basis for a predictive model and optimization strategy. Unlike experimental data, which typically targets collecting a subset of data, the FEM model provides insight within the complete specimen and the surrounding

environment / substrate. However, experimental research must be performed to calibrate the simulation models over the problem space, as there is no comprehensive body of knowledge to draw upon for metal AM processes. Consequently, once a calibrated simulation model is developed, it is essential to extract information not only at the nodes, but the gradient data in the regions between the nodes (Fig. 4 (a)) – in 3D (Fig. 4 (b)). In Fig. 4 (a) there are seven distinct internal residual stress levels within one mesh region, and it is evident from Fig. 4 (b), that the variations in stress are significant along the bead. Therefore, it is proposed to perform data digitization and curve extraction to identify key regions and use this information to seed comparative and predictive models. The simulation results need to be extracted and transformed into a format that will serve as the basis for the comparison and prediction model solution approaches under development.

Multiple available commercial digital image and CAD tools were explored to determine whether an automated solution existed for extracting contours or generating topology maps, based on grayscale or color images. The grey scale value at each pixel is converted into a z height, and some smoothing occurs between these points, but the pixilation influence is evident, as there is graininess in the image (Fig. 5 (a) and (b)). Rhino® has a raster to topology converter for grayscale images, and the color image can be overlaid, as shown in Fig. 5. There are ripples in the surface, and in regions where there should be distinct height differences (yellow and orange), there are not, as the grayscale pixel values vary between 228 and 232, and are not distinguishable for a pincushion based surface. After converting Fig. 4 into grayscale, the boundaries can be detected, but the boundaries are not as clearly distinguishable, and it appears that the detected boundaries could correlate to more than one stress level when they are extracted with the GIMP edge detection algorithm.

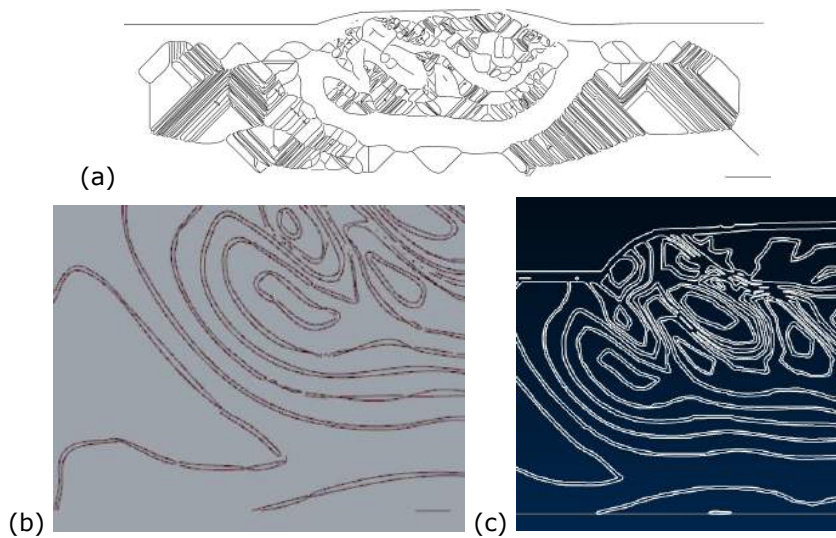


**Figure 4:** (a) cross section AA and the seven residual stress boundaries within one mesh region bounded by 4 nodes, (b) 10 cross sections for a single bead.



**Figure 5:** (a) Rhino raster - topology conversion results, (b) detailed view showing localized ripples and lack of distinctive heights, (c) gray scale representation and boundaries detected for the boxed region in Fig. 4.

Existing raster to vector conversion software for CAD geometry results required grayscale images, and they resulted in interesting patterns when the grayscale FE images are used directly (Fig. 6 (a)). When seeded with grayscale images preprocessed by GIMP - edge detect, the exterior boundaries were traced (Fig. 6 (b) and (c)), or intersecting lines resulted (Fig. 6 (d) and (e)). Note: All these results are for the 50% overlap configuration B scenario.



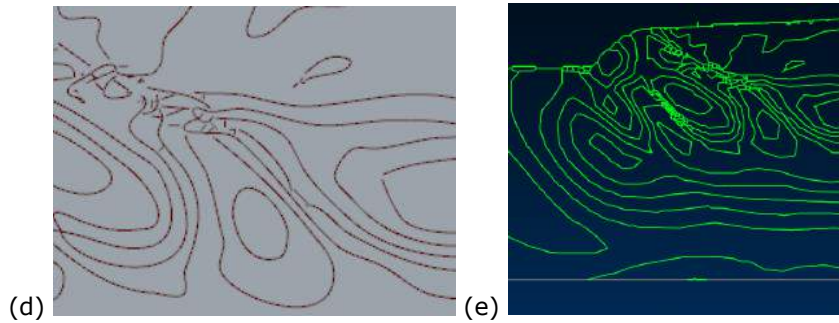


**Figure 6:** (a) Rapidresizer [13] results (b) external boundary lines traced using Rapidresizer (viewed in Rhino®), (c) external boundary lines traced using the Vectorization.org [21] tools (viewed in Mastercam ®), (d) intersecting lines result (Rapidresizer viewed in Rhino®), (e) Raster to Vector Software [14] (viewed in Mastercam ®).

Based on reviewing several raster-to-vector solutions, it was determined that manually tracing boundaries using CAD tools needs to be the approach taken at this time. Preprocessing will be performed using GIMP software to extract the boundaries and manipulate the image for brightness and contrast to facilitate the tracing process. The data transformation methodology is described in detail in the next section.

### 3 METHODOLOGY

The overall approach to develop faster predictive models is to proceed from experiments, to calibrated FEA models, to a trained black box solution leveraging patterns observed from these analyses. The FEA and experimental results need to be reformatted into a data set approach for a black box model. Simple single bead experiments, multi-bead experiments for one layer, stacked beads (one bead thickness), and multi-bead and multi-layer experiments have been done for 420 stainless steel. Single bead finite element models were developed for all the experimental configurations shown in Table 1. For a three bead single layer scenario, finite element model results are derived for 9 configurations, which are presented in Table 3, and sample results are illustrated in Fig. 7. In addition to comparing the single bead simulation results to the residual stress experimental results, hundreds of Vickers micro hardness results were collected for the single and multiple bead scenarios for the 40%, 50%, and 60% overlap configurations. The experimental and simulated hardness data correlate well [9, 10]; consequently, simulated residual stress data for the three-bead configurations are employed.

<b>40%, 50%, 60% overlap</b>	<b>A</b>	<b>B</b>	<b>C</b>
Powder feed rate (g/min)	20	20	20
Laser power (KW)	2.5	2.5	2
Focal length of lens (mm)	400	400	400
Laser speed (mm/S)	10	12	12

**Table 3:** Multi-bead process parameters and overlap configurations used for the FEA models.

It is readily evident that the magnitudes and positions of the stress regions vary, and that the observed stress patterns for the multiple bead configurations are significantly different from the single bead configuration. No symmetry of the stress patterns is observed for the three bead scenario, there is a limited tensile stress region in the deposited beads (between bead 1 and 2), and

the maximum tensile stress regions appear to be in the bead overlap regions deep in the substrate, not along the center of the bead.

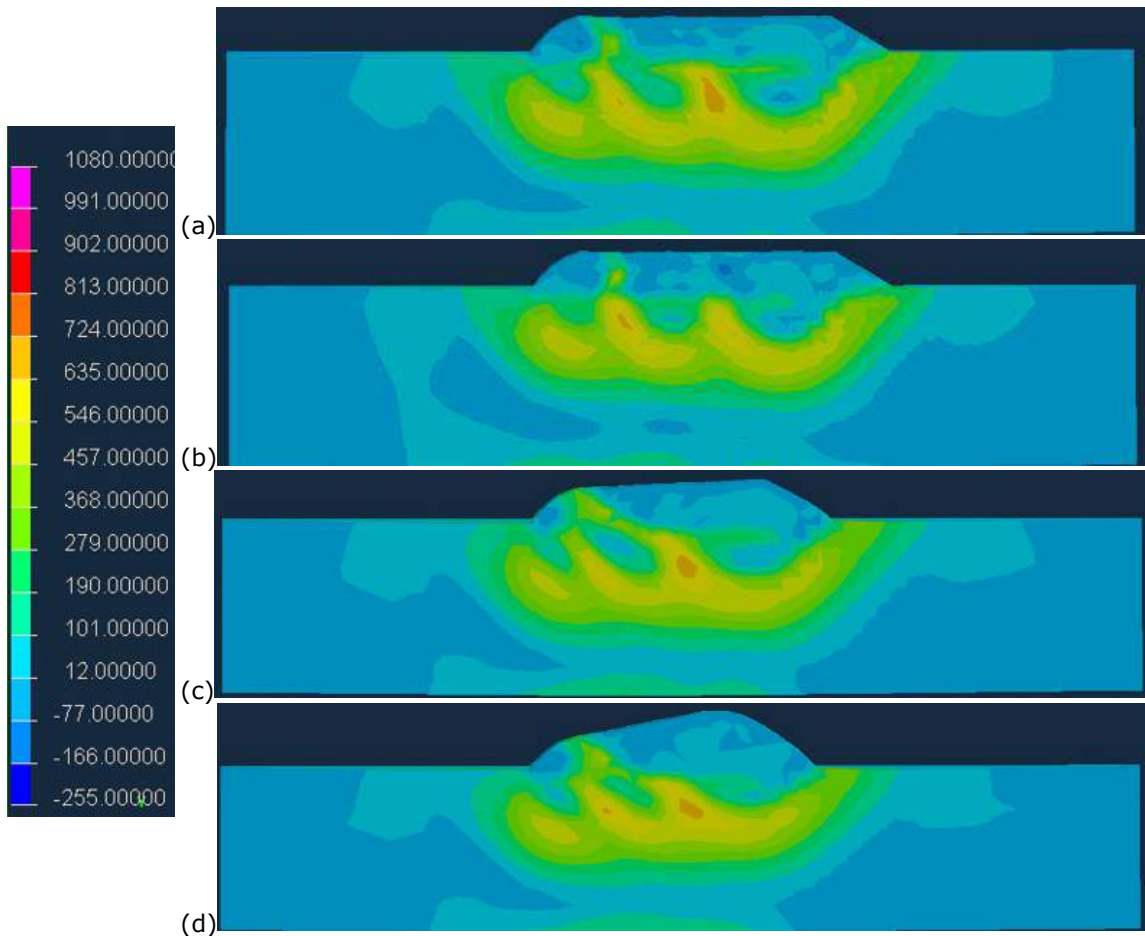


**Figure 7:** Residual stress scale, and the results for 40% overlap for experiment A (a) and C ((b), 50% overlap experiment A (c), and 60% overlap experiment A (d).

A comprehensive data set is required for developing meaningful predictive models. Consequently, the boundary regions for the induced residual stresses need to be determined, and intermesh data points and the residual stress value at each point extracted in a structured manner. A topology-based approach is investigated to generate the training data required to teach a black box model. The file format for the black box model for the input will be the process settings 1..i, and the output will be:

$x, y, z$ , *physical property (residual stress for this research)*,

where  $x, y, (z)$  are the Cartesian coordinates,

*physical property* is the property to be considered, i.e., induced residual stresses, hardness, etc.

In Fig. 8, the ANN architecture for the initial black box solution is illustrated. There are 3 hidden layers, with the neurons for layer 1, 2, and 3 being 20, 10, and 10 respectively.

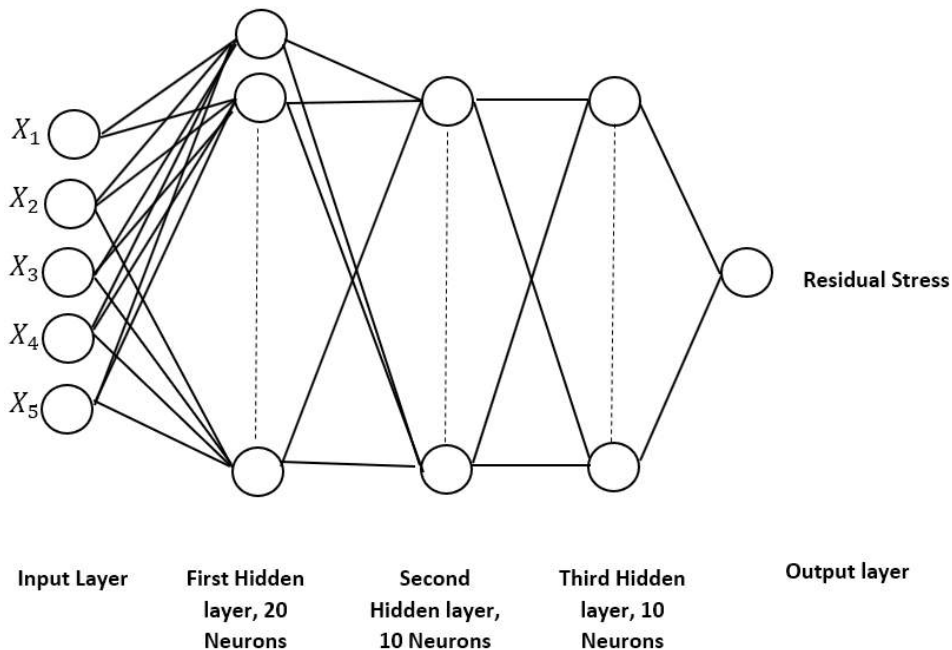


**Figure 8:** Artificial neural network architecture for the initial black box solution, where  $X_i$  is a process setting.

As topology creation solutions in Rhino© (or other image to CAD conversion software tools) do not isolate each bounded region well, the methodology and tools for proposed here are:

- Employ a common scale for the iso curves / heat map colors and the FEA model geometry
- Extract the boundary contours (GIMP) for the heat maps (Fig. 9 (a) and (b))
- Create NURB curves (Mastercam®) from the boundary curves (isolines or GIMP solution)
- Create extruded solid models of the regions, where each solid model color correlates to a stress, and compare the models developed from the various process configurations (Mastercam®) (Fig. 9 (c)).
  - Use solid modeling tools to determine 'difference' regions or to assess size/centroid metrics
  - Create surfaces and point data for prediction and comparison modelling
- Create Voronoi diagrams and extract medial lines from the boundary curves and compare results (Rhino© and Grasshopper© tools) (Fig. 9 (d)).

The boundary curves created from an image may have some noise as shown in Fig. 9 top; consequently, a filtering configuration needs to be established for this process to be automated. However, once the geometry is created, detailed analytical comparisons can be performed. With a unit extrusion height, the dimensions, size, and centers of each stress region can be determined using standard solid model analysis tools which are then correlated to the bead geometry.

Employing a unique height for each solid region and trimming the geometry at selected planes will allow for users to create residual stress and residual stress rate change profile curves with respect to the desired Cartesian coordinates, which can be used to seed a black box predictive modeling solution.

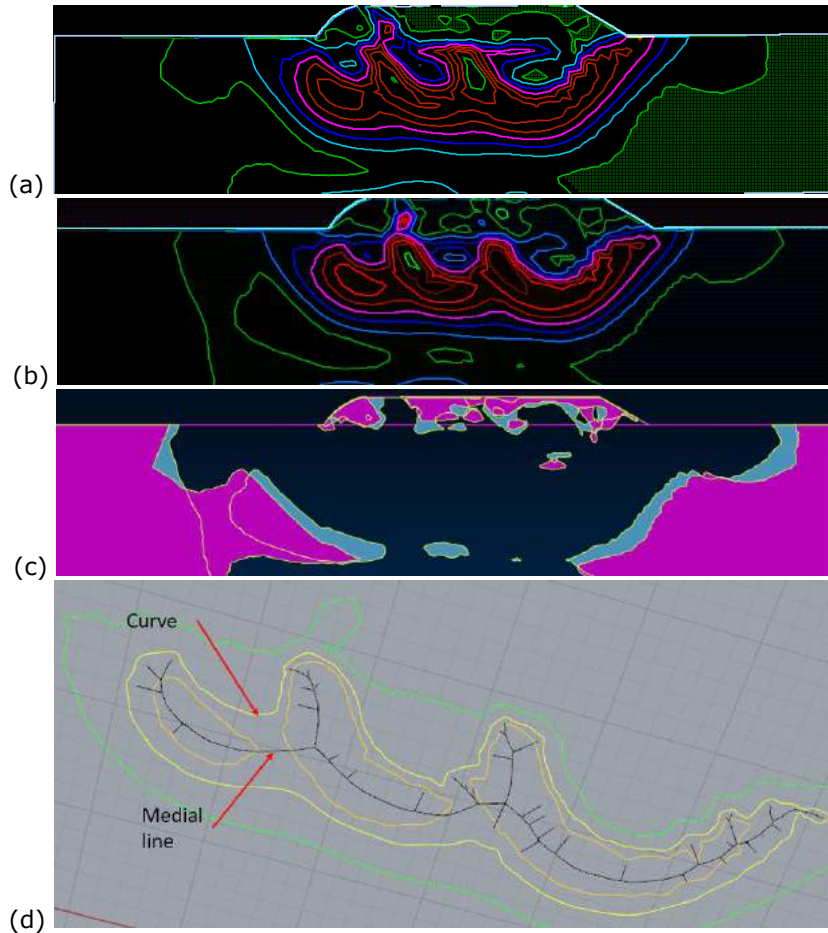


**Figure 9:** Residual stress boundary curves for the 40% overlap for experiment A (a) and C (b), and boundary curves solid model overlay for the low stress regions (c), and medial line for the selected curve (d).

Two procedures are explored to generate overarching geometric model comparisons, as shown in Fig. 10. The same graduated color scale, and the same geometric scale must be employed. Once the contour geometry is created, simple extruded solid models are created. Each residual stress 'bin' (Fig. 7) is assigned an extrusion value, where the regions with the lowest residual stress value are extruded one unit. A unit increment for the extrusion height to residual stress bin is employed (Fig. 11). This is the same initial step for both options.

For option 1, a slicer module designed for additive manufacturing (APlus®) is used to create slice contours. Boolean join operations need to be performed prior to slicing to reduce redundant / colinear geometry (Fig. 12 (a)). Once the slice contours are created (Fig. 12 (b)), end points can be readily created (Fig. 12 (c)). To create a grid of points, slicing must occur in the front and side construction planes. Filtering is required to extract the highest points and eliminate redundant data.

For option 2, once the solid models are created, an array of points is projected onto the top of the surfaces, as shown in Fig. 13 (a) and (b). A grid of points is generated using standard geometry translation tools. This controls the point density or the predictive model resolution. Then, a 'project point' transformation is performed. Again, filtering is performed to remove redundant data. This is the method employed in this research to extract the residual stress data from the FEA results and

seed the black box models. These points are saved into a \*.csv file, where one column (the 'z' coordinate) is a representative residual stress value.

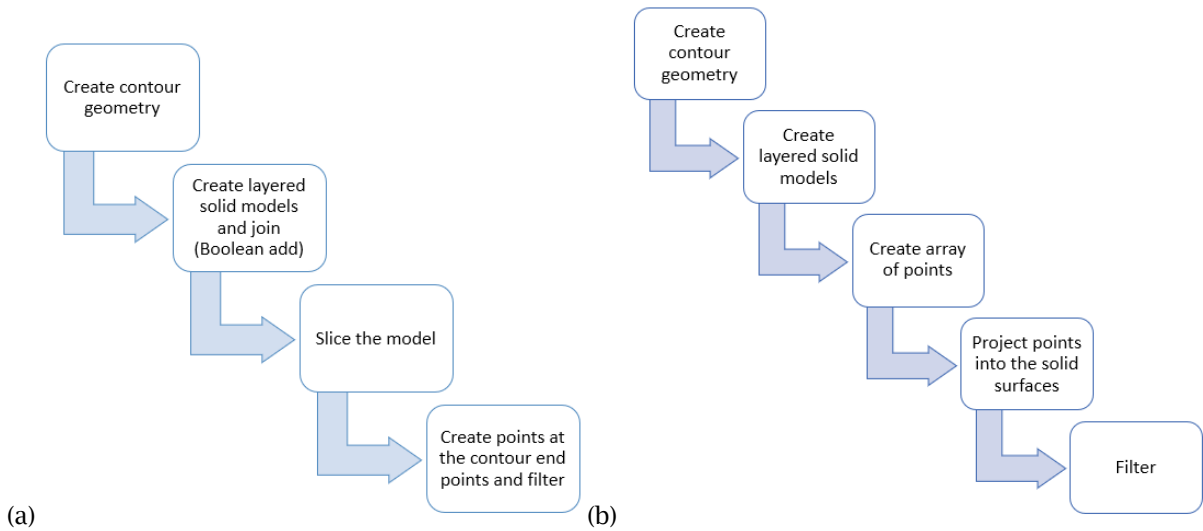


**Figure 10:** (a) Option 1 process flow, (b) option 2 process flow.

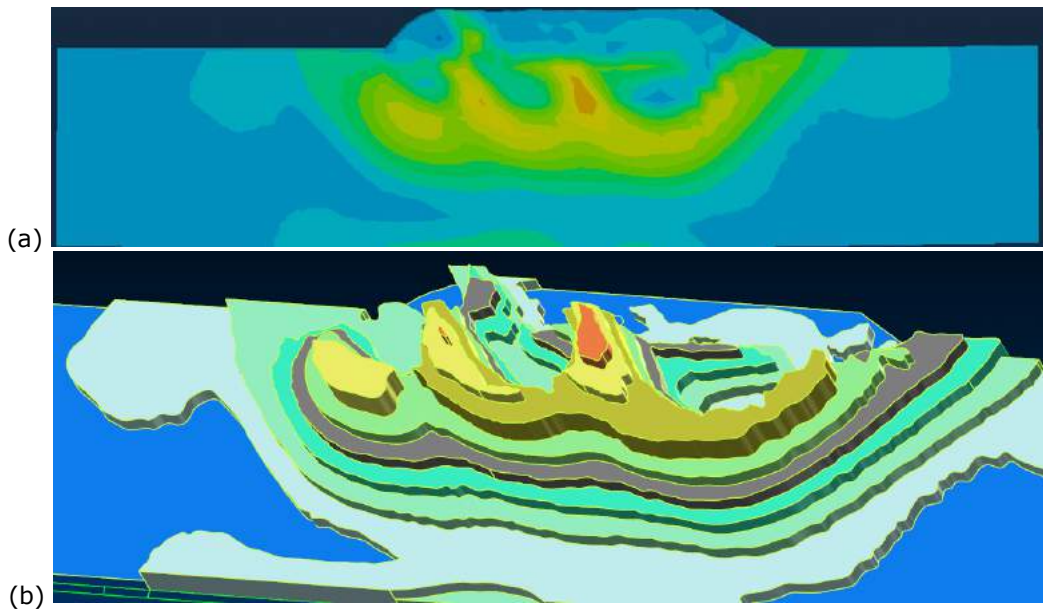


**Figure 11:** (a) Heat map, and (b) solid models with each layer height corresponding to a color region from the heat map.

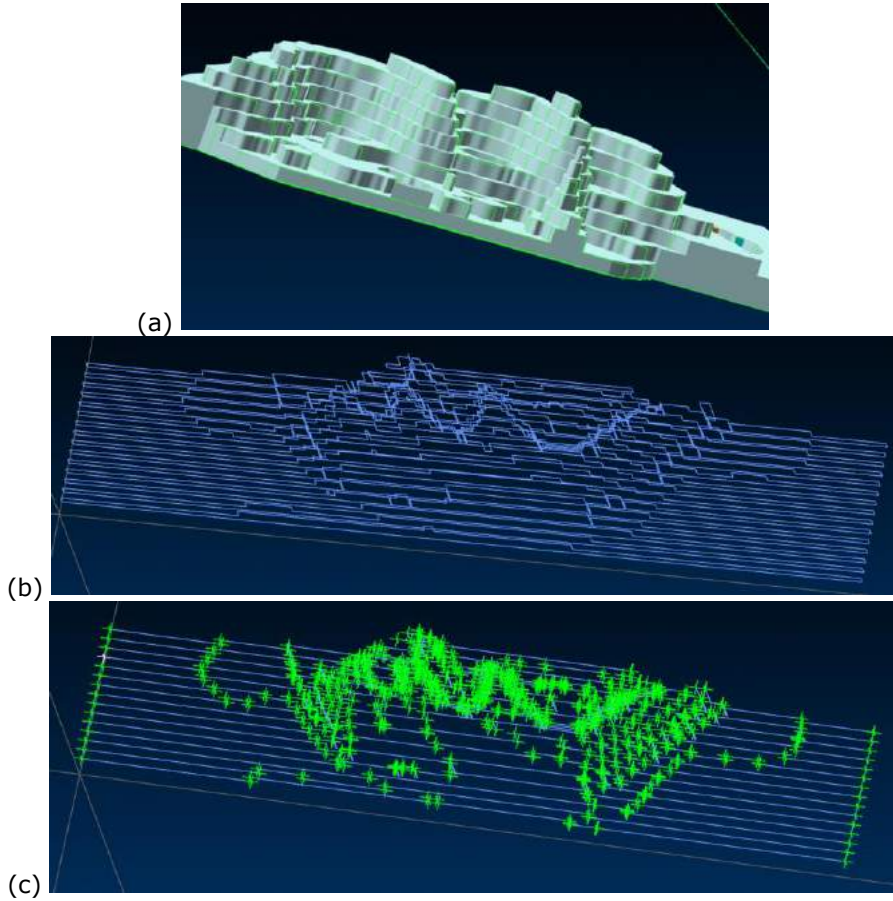


**Figure 12:** (a) Solid model, (b) slice contours (Front view), and (c) end points.

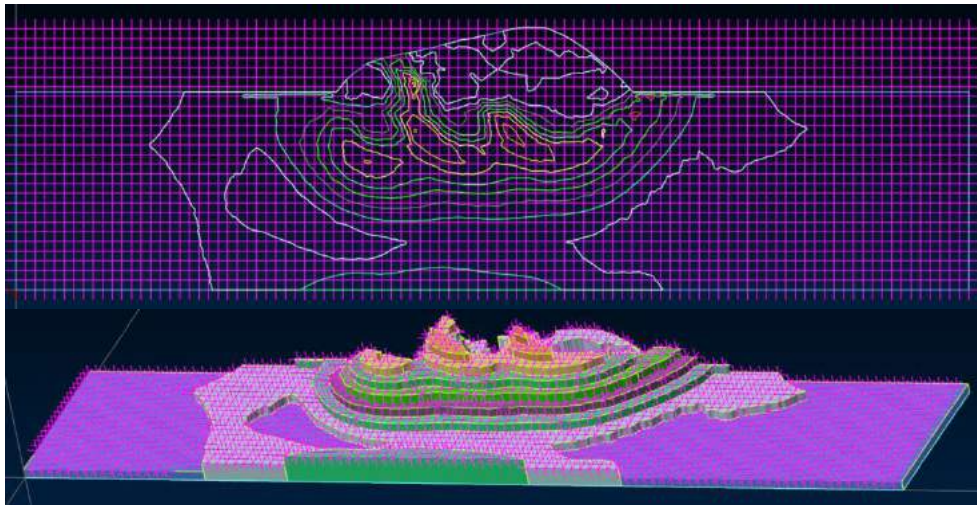


**Figure 13:** (a) Point set, and (b) points projected onto the top surfaces.

Various comparison methods are utilized – both digital and geometric approaches are considered. Several GIMP tools allow for a difference or subtraction between image layers. The difference mode subtracts the pixel value of the upper layer from that of the lower layer and then takes the absolute value of the result; whereas, the subtract mode subtracts the pixel values of the upper layer from the pixel values of the lower layer. The difference mode is used here, as the subtraction mode resulted in a dark (near black) image. The intensity is changed for the color scale difference mode results for ease of interpretation (Fig. 14). The variability and the characteristics of the overlap regions are complex. A gray scale image is extracted as well, as this reduces the model complexity for deep neural network modeling (Fig. 15). However, this generated inconsistent stress data, as each color corresponds to a distinct stress value range, but the gray scale value could be the same for two (or more) stress values due to the loss of information.

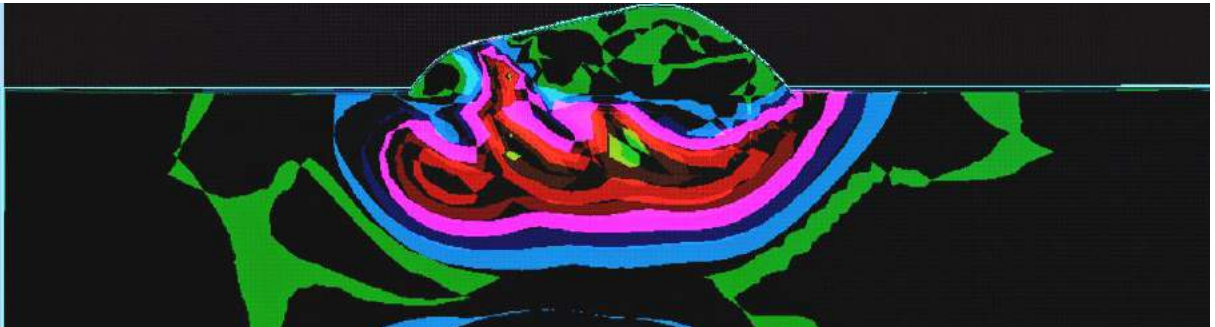


**Figure 14:** Difference between scenario 60 A and 60 C – the black regions indicate no difference.



**Figure 15:** Grayscale difference between scenario 60 A and 60 C – the black regions indicate no difference.

To create a 3D model for a stress region, multiple cross sections are used along the bead, and lofting surface models are created, with end caps. Using these surface models, either additive (raster scan) or subtractive (pocketing) tool paths can be created, saved as geometry, and points positioned within these line/spline segments. Each point corresponds to an  $x, y, z$  position for a stress value.

The results for these approaches are discussed in the next section. The extracted data is employed to develop an artificial neural network (ANN) (Fig. 8), and an adaptive neuro fuzzy interference system (ANFIS) solution. Initial results are reported for the ANN in this work. This research is in its preliminary stages.

## 4 RESULTS

The GIMP edge detect filter extracted the boundaries and used a consistent color set for each region. Regions that were consistently problematic for the images being utilized are highlighted in the boxed areas (Fig. 16). Converting the image data into geometry introduces a scaling factor that must be taken into consideration when extracting and comparing the results to physical data. The results are consistent to themselves, but the geometric values in the plots are amplified.

Employing option 1 to create a point cloud data at the stress region edges allows for some data analysis to be performed. The changes in the stress values at different Y intervals is shown in Fig. 17 (a). Residual stress differential values can also be plotted to determine the rate of change of the stresses (Fig. 17 (b)). Comparisons between samples could not be readily performed without interpolating values.

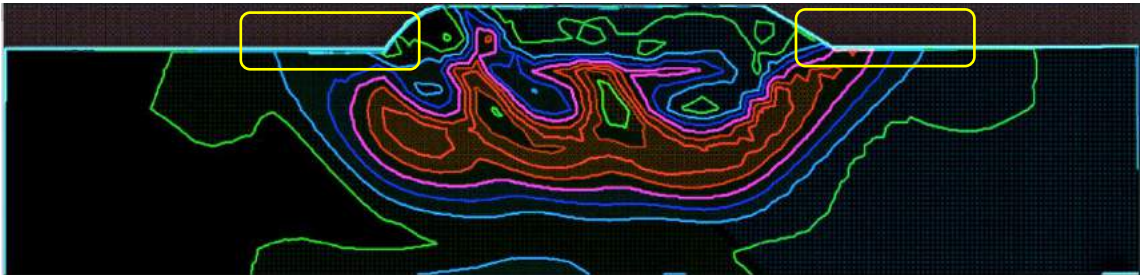


**Figure 16:** Regions where multiple boundaries converge.

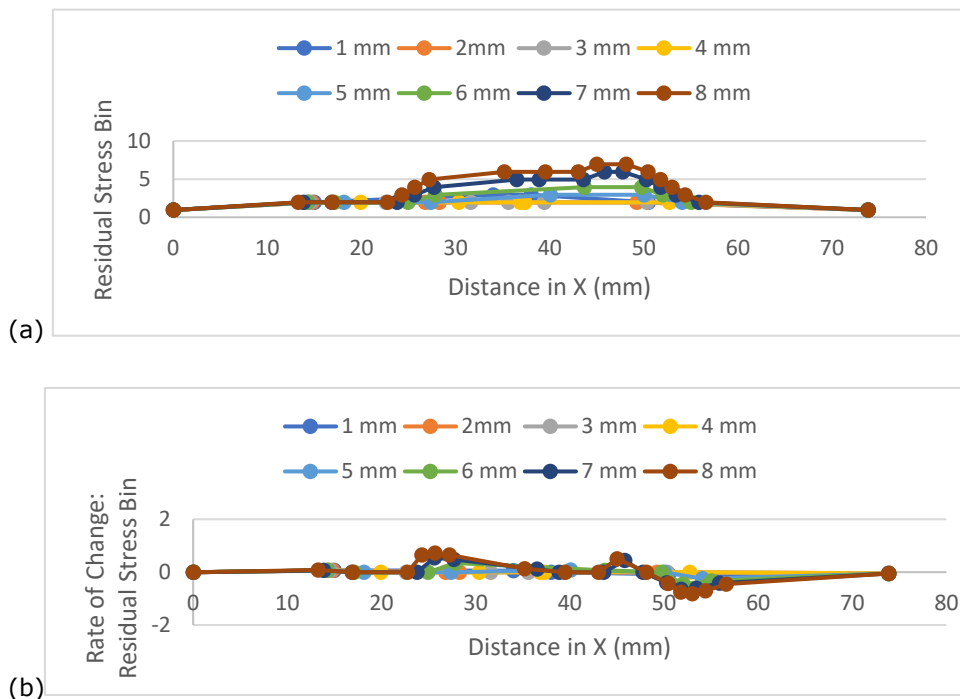


**Figure 17:** (a) Residual stress curves for selected Y values for sample 40 A, and (b) rate of change for residual stress values.



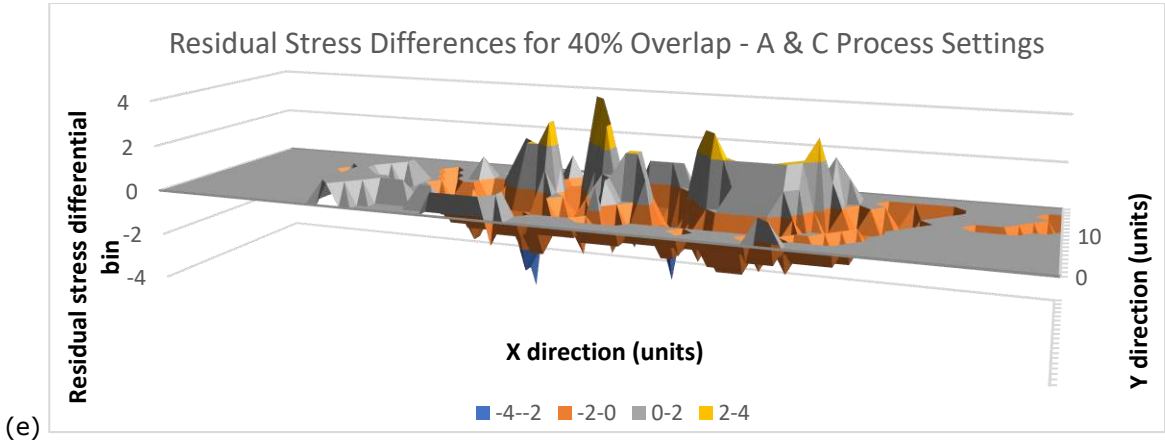


**Figure 18:** (a) A surface map for sample 40 C using the Excel data, and (b) conditionally formatted data map for sample 40 C, (c) conditionally formatted data map for sample 40 A, (d) conditionally formatted data map for the data differences, and (e) a surface map of the residual stress differences.

There are bead geometry differences with the various scenarios being explored. Attention to scaling and the reference datum point must be made, and the regions with no overlapping geometry identified, as shown in Fig. 19 (boxed areas), which illustrates the 40 B to 60 B comparison. The magnitude and location shifts for the percent overlap differences for the high tensile and compressive stress regions are readily identified.

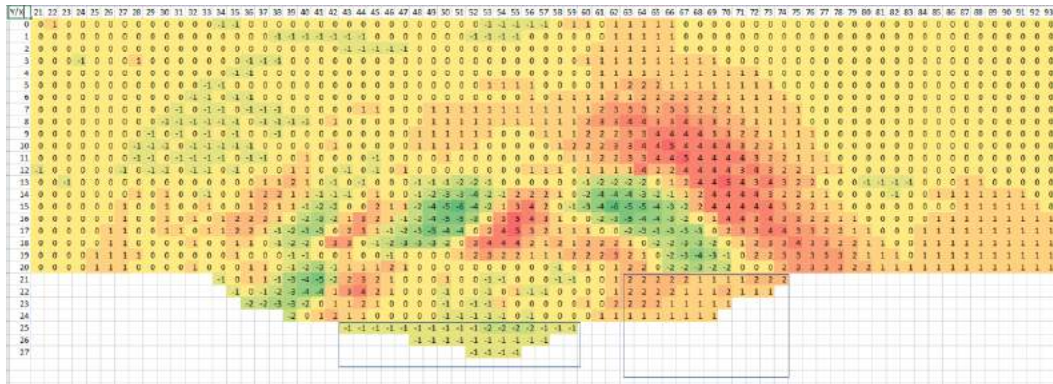


**Figure 19:** (a) Residual stress difference data for scenario 40 B – 60 B.

When doing a simple cell count enumeration and comparing the total cells for each stress level for the 40 and 60 percent overlap conditions for the B process settings, the counts are very similar (Fig. 20), reinforcing that the percentage overlap is a key concern as well as the process settings.

Geometric analyses for the width, height, area, centroid positions, and so forth can be determined from the curve geometry for the various configurations. A sample is shown in Table 4.

When developing a methodology to capture 3D positional and stress data, multiple cross sections along the deposited bead need to be transformed into geometry. The curves can vary in shape and position (Fig. 21 (a)), and the sections are not constant in shape. (Fig. 21 (a)). Surface or solid models bounding a stress region can be derived from these boundary curves (Fig. 21 (b) and (c)), and it can be seen that the highest tensile region boundary shape fluctuates along the length of the

bead. Multiple cross sections are required at the start and stop areas to capture the stress region shapes. Once a surface or solid model region is generated (lofted, swept, and flat end cap surfaces), tool paths can be developed, saved as geometry, and then points positioned along the tool path geometry, creating a 3D point cloud for that stress region. Here an AM tool path for laser cladding is used to create the tool path geometry that is illustrated in Fig. 21 (d).

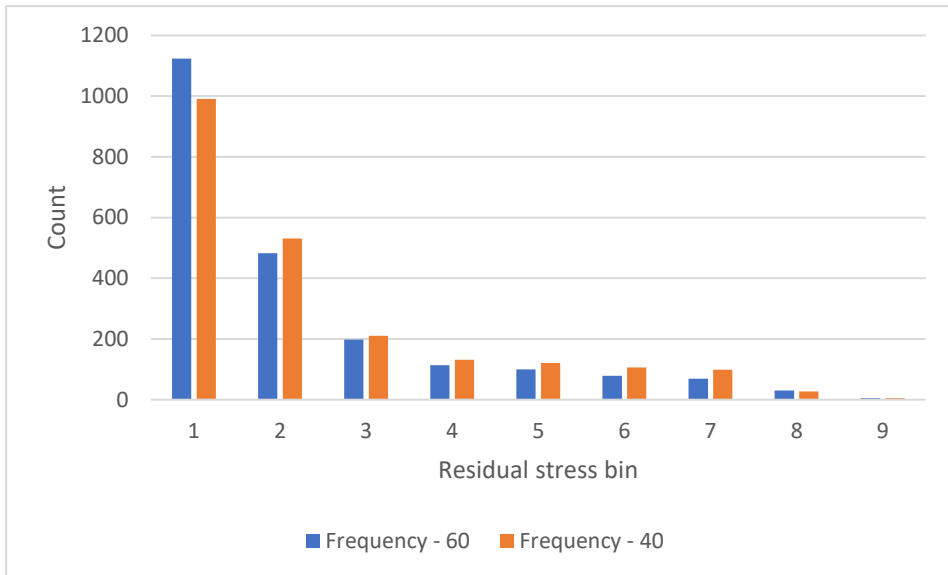


**Figure 20:** Residual stress bins data for scenario 40 B and 60 B.

Configuration	Normalized stress value	No. of Regions	Perimeter	Area	Centroid
50 A	10	1	7.82	3.96	48.72, 14.19
50 B	10	1	7.83	3.87	49.16, 14.24
50 A	7	3	3.08	0.30	39.88, 20.48
			12.25	6.87	34.22, 12.13
			104.43	67.00	50.18, 11.95
50 B	7	2	12.39	6.14	34.88, 11.72
			104.93	66.63	50.69, 12.03
60 C	7	3	16.08	13.29	36.66, 13.33
			103.56	48.77	49.97, 14.71
			2.09	0.18	61.03, 16.25

**Table 4:** Comparison of stress region characteristics for selected configurations.

When using the point cloud data extracted from the images, initial neural network predictive results are promising. As shown in Fig. 22, the regression plots for a node-based data set (Fig. 22 (a)), and the digital data seeded model (Fig. 22 (b)). The regression values are significantly higher for all elements when using the data extracted from the image transformation process done here.

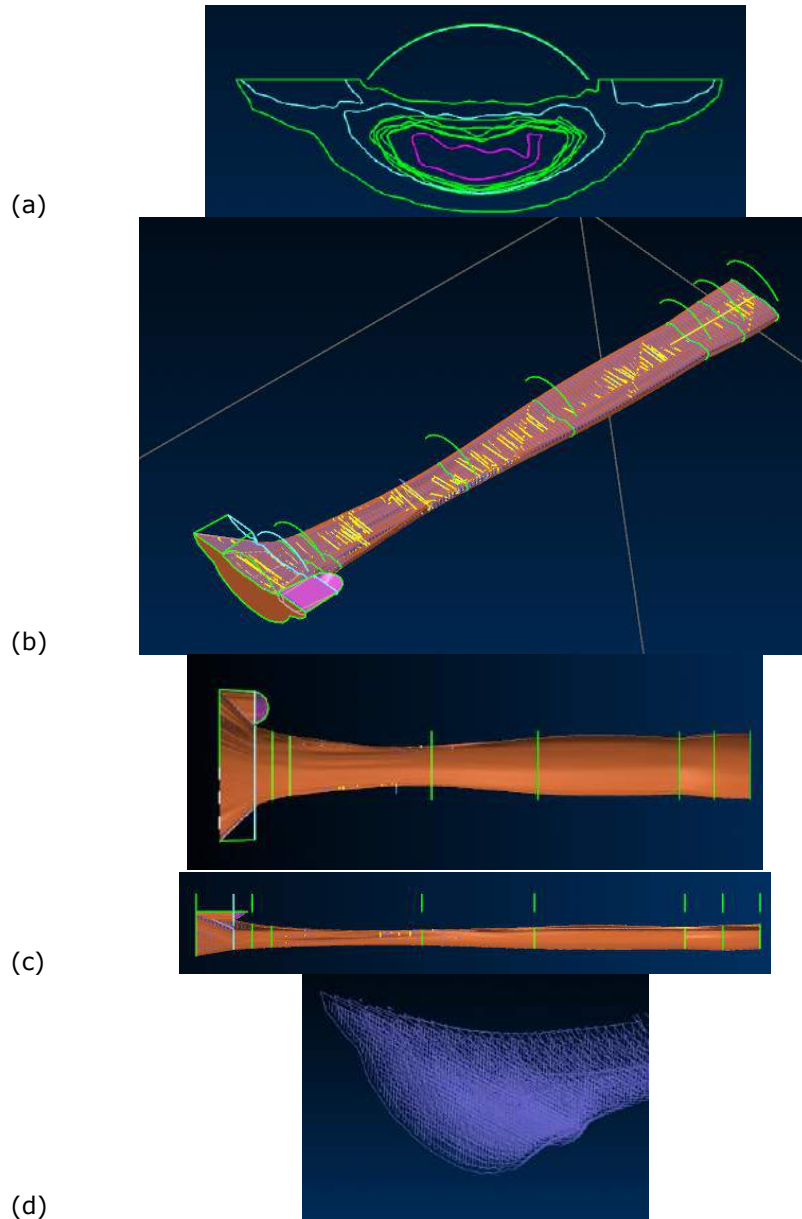


**Figure 21:** (a) Highest tensile stress residual stress boundary curves along bead 'experiment A', (b) 3D view and (c) front and right side views showing the high tensile stress region shape, and (d) AM tool path geometry which can be used to generate a point cloud data set.

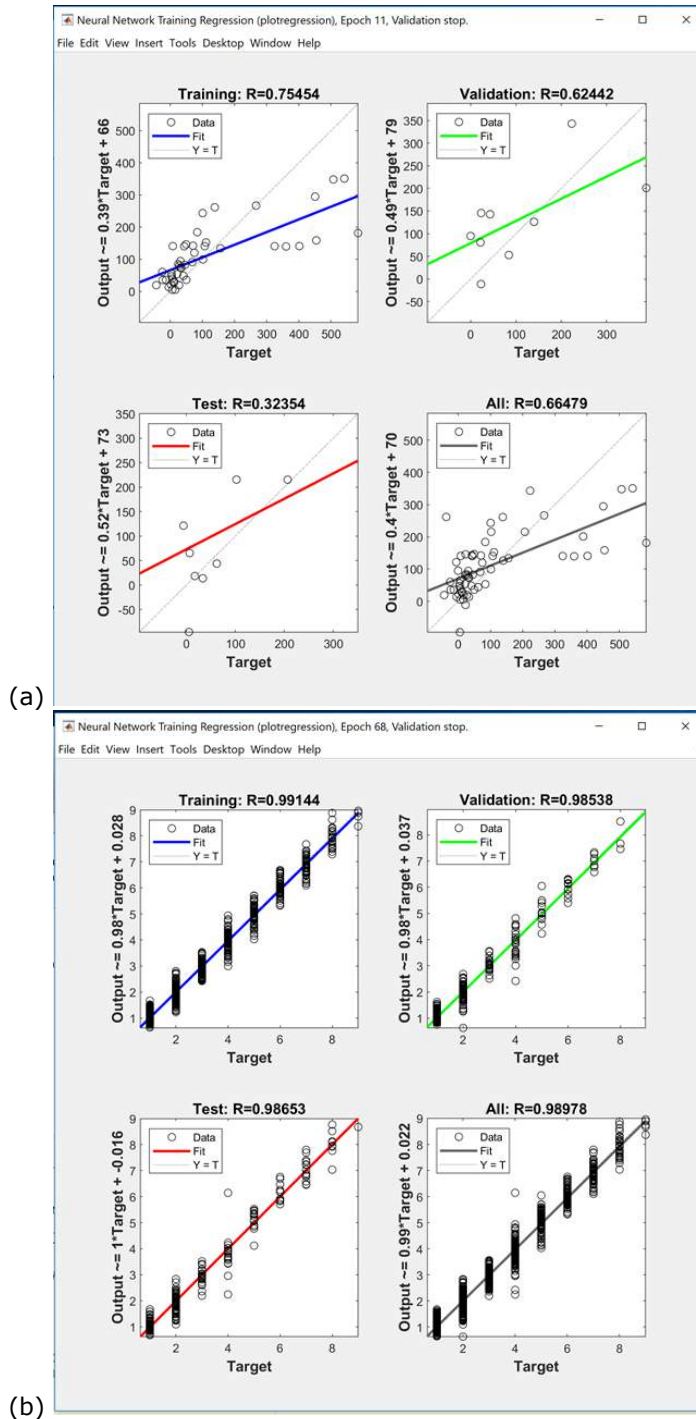


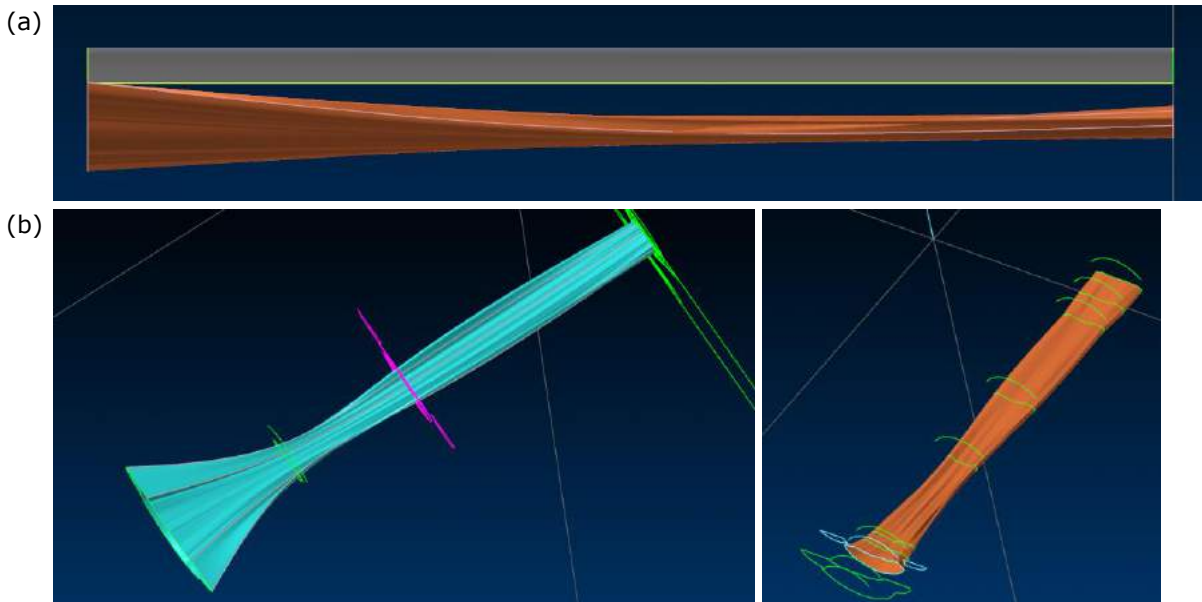
**Figure 22:** Preliminary artificial neural network model results using (a) node data, and (b) topology/image data.

## 5 DISCUSSION

The AM process family has been introduced relatively recently. Therefore, experimental analyses, microstructure evolutions research, tools to model and predict behaviors, and developing best practices are being determined concurrently. The heat maps generated from the FE results have information complementing the data at the nodes, how is this information can be extracted and leveraged is the key question addressed in this research. Although no automated solution could be readily determined, the foundations are available to semi-automate a solution, allowing researchers to extract additional data and knowledge from the residual stress simulation results. This is important, as there are significant amounts of data to collect as there are transient conditions and variations in overlap percentages which influence the final build results. The granularity of the collected data, the number of images to be utilized, and the influence of discretizing the data need to be explored further. This methodology can be employed for 2D comparisons, such as the residual stresses in a specific region, or a 3D based point cloud-residual stress (or other property such as hardness) data set can be generated and used for modeling. Once the 2D point cloud set with the discretized data is generated, the data set can be used to seed a neural net model.

Specific geometric data can be extracted from the contour and surface data, and using the Rhino® and Grasshopper® tool box, Voronoi diagrams and medial lines can be extracted. However, the basis for comparing medial line data has not been determined at this time.

The number of cross-sections influences the 3D model results for determining a 3D stress region. As shown in Figure 23, the number of cross sections change the stress regions boundary. For the highest tensile stress, three cross sections (Fig. 23 (a)) provide a different those shown in Fig. 21. This is emphasized in Fig. 23 (b). However, multiple 3D regions can be determined (Fig. 23 (c)), therefore, 3D point cloud – stress data sets can be generated.



(c)

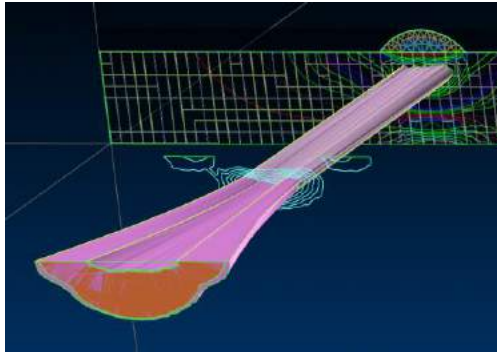
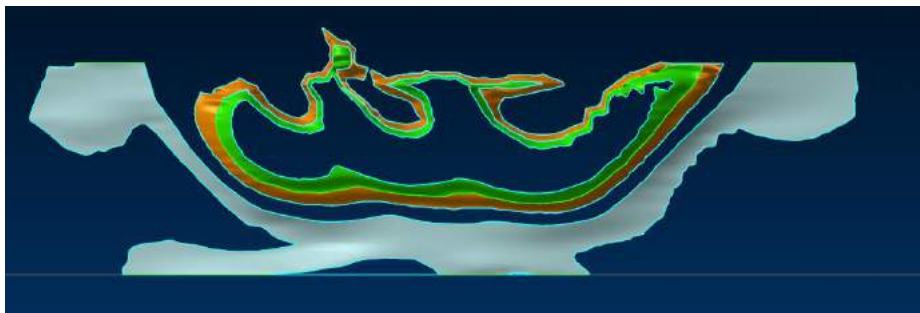


**Figure 23:** (a) Stress regions developed from 3 cross-sections – a bead model is included as a reference (b) a comparison of 3 and 8 cross-sections to model the high tensile stress regions, and (c) 3D model of two tensile regions.

Automating the solution approaches, determining the number of cross sectioning images required to represent the residual stress conditions, and developing an optimization model considering the geometry and physical properties are challenges to be addressed in the future work. Difference contours need to be extracted from the comparison data. In addition to these items, CAD tools to facilitate developing a topological model that is not 'piecewise' linear steps needs to be determined. The standard surface modeling tools introduces folds and wrinkles if the sync points are incorrect (Fig. 24). However, developing predictive models using a machine learning approach with experimental and simulation activities is challenging, and various approaches to seed a model must be explored to determine a robust and extendable approach.

(a)



(b)

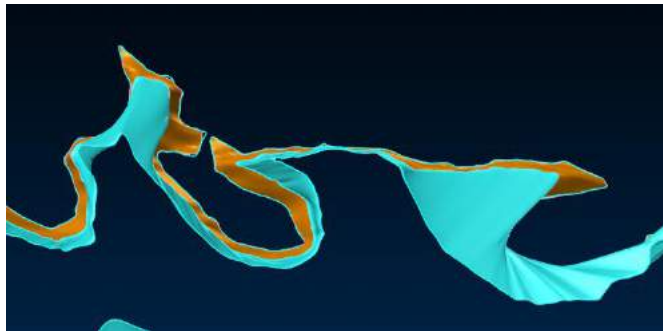


**Figure 24:** (a) Surface models to create a continuous model solution, and (b) challenging geometry that results in folds, wrinkles, and distortions.

## 6 CONCLUSIONS AND FUTURE WORK

AM fabrication challenges focus not only on fabricating components with the desired geometry, but also with the desired performance characteristics. Confidence in the mechanical and physical properties for AM components is required. Durability and performance are related to the manufacturing residual stresses. An effective predictive model cannot focus on absolute maximum and minimum stress magnitudes, but must include intermediate values and their positions, as well as the input process parameters and the tool path information (direction, percentage overlap). Therefore, a standardized method for direct comparisons needs to be determined for any  $x,y,z$  coordinate, as well as the observed residual stress patterns. This research proposed converting the results models into topology and 'raster' data via contour extraction and solid modeling tools to extract residual stress values (and changes in residual stress) patterns as well as creating medial lines that could be used for pattern recognition purposes. This data can be used as an input for training artificial neural network models, or other AI strategies.

The quality of a black box predictive model is highly dependent on the amount of data, as well as the data characteristics. Shape comparison strategies must be performed, and the influence on the point cloud density on accuracy and run time need to be explored. An adaptive neuro fuzzy interference system solution is to be developed as well as an ANN using the same training and validation data. There are several transient conditions that need to be considered for a robust predictive model. The amount of data, the flexibility and extensibility of this black box solution approach needs to be determined to address these various conditions.

To conclude, product and process designers need to determine 'design for additive manufacturing' and effective build solutions for cost effective, functional components. The influences of the component shape, build material(s), process settings, and the tool path settings need to be considered. Solution approaches need to fuse experimental and simulation data with sophisticated predictive modeling tactics to achieve this goal. The data transformation methods proposed here will translate FEA results into a flat data file that can readily be used for training a black box model.

## 7 ORCID

(Ruth) Jill Urbanic, <http://orcid.org/0000-0002-2906-7618>

Bitā Mohajernia, <http://orcid.org/0000-0001-7119-2490>

Navid Nazemi, <http://orcid.org/0000-0001-8464-6690>

## REFERENCES

- [1] Aggarwal, K.; Urbanic, R. J.; Saqib, S.: Development of predictive models for effective process parameter selection for single and overlapping laser clad bead geometry, *Rapid Prototyping Journal*, 24(1), 2018, 214-228. <https://doi.org/10.1108/RPJ-04-2016-0059>.
- [2] Balu, P.; Hamid, S.; Kovacevic, R.: Finite element modeling of heat transfer in single and multilayered deposits of Ni-WC produced by the laser-based powder deposition process, *Int. J. Adv. Manuf. Technol.*, 68, 2013, 85-98. <https://doi.org/10.1007/s00170-012-4710-2>.
- [3] El-Cheikh. H.; Courant, B.; Branchu, S.; Hascoet, J.; Guillen. R.: Analysis and prediction of single laser tracks geometrical characteristics in coaxial laser cladding process, *Optics and Lasers in Engineering*. 50(3), 2012, 413-422. <https://doi.org/10.1016/j.optlaseng.2011.10.014>.
- [4] Chew, Y.; Pang, J.; Bi, G.; Song, B.: Thermo-mechanical model for simulating laser cladding induced residual stresses with single and multiple clad beads, *Journal of Materials Processing Technology*, 224, 2015, 89-101. <https://doi.org/10.1016/j.jmatprotec.2015.04.031>.

- [5] Fallah, V.; Alimardani M.; Corbin, S. F.; Khajepour, A.; Temporal development of melt-pool morphology and clad geometry in laser powder deposition, *Comp Mater Sci.*, 50, 2011, 2124-2134. <https://doi.org/10.1016/j.commatsci.2011.02.018>.
- [6] Farahmand, P.; Kovacevic, R.: An experimental-numerical investigation of heat distribution and stress field in single- and multi-track laser cladding by a high-power direct diode laser, *Optics & Laser Technology*, 63, 2014, 154-168. <https://doi.org/10.1016/j.optlastec.2014.04.016>.
- [7] Goodarzi, D.; Pekkarinen, J.; Salminen, A.: Analysis of laser cladding process parameter influence on the clad bead geometry, *Welding in the World*, 61(5), 2017, 883-891. <https://doi.org/10.1007/s40194-017-0495-0>
- [8] Khanzadeh, M.; Chowdhury, S.; Marufuzzaman, M.; Tschopp, M. A.; Bian, L.; Porosity prediction: Supervised-learning of thermal history for direct laser deposition, *Journal of Manufacturing Systems*, 47, 2018, 69-82. <https://doi.org/10.1016/j.jmsy.2018.04.001>.
- [9] Nazemi, N.; Urbanic, R. J.: A numerical investigation for alternative toolpath deposition solutions for surface cladding of stainless steel P420 powder on AISI 1018 steel substrate, *International Journal of Advanced Manufacturing Technology*, 96(9-12), 2018, 4123-4143. <https://doi.org/10.1007/s00170-018-1840-1>.
- [10] Nazemi, N.; Urbanic, R. J.; Alam, M.: Hardness and residual stress modeling of powder injection laser cladding of P420 coating on AISI 1018 substrate, *International Journal of Advanced Manufacturing Technology*, 93, 2017, 3485. <https://doi.org/10.1007/s00170-017-0760-9>.
- [11] Palumbo, G.; Pinto, S.; Tricarico, L.: Numerical finite element investigation on laser cladding treatment of ring geometries, *J Mater Process Technol*, 155-156, 2004, 1443-1450. <https://doi.org/10.1016/j.jmatprotec.2004.04.360>.
- [12] Proto Manufacturing <https://www.protoxrd.com/>.
- [13] Rapidresizer: <https://online.rapidresizer.com/tracer.php>.
- [14] Raster to Vector Software: <https://www.raster-vector.com/>.
- [15] Saqib, S.; Urbanic, R. J.: Investigation of the Transient Characteristics for Laser Cladding Beads using 420 Stainless Steel Powder, *ASME Journal of Manufacturing Science and Engineering*, 139(8), 2017, 081009. <https://doi.org/10.1115/1.4036488>.
- [16] Song, M.; Lin, X.; Yang, G.; Cui, X.; Yang, H.; Huang, W.: Influence of forming atmosphere on the deposition characteristics of 2Cr13 stainless steel during laser solid forming, *Journal of Material Process Technology*, 214, 2014, 701-709. <https://doi.org/10.1016/j.jmatprotec.2013.09.023>.
- [17] SYSWELD: ESI-Group (2015) SYSWELD 2015 reference manual
- [18] Toyserkani, E.; Khajepour, A.; Corbin, S.: 3-D finite element modeling of laser cladding by powder injection: effects of laser pulse shaping on the process, *Optics and Lasers in Engineering*, 41, 2014, 849-67. [https://doi.org/10.1016/S0143-8166\(03\)00063-0](https://doi.org/10.1016/S0143-8166(03)00063-0).
- [19] Toyserkani, E.; Khajepour, A.; Corbin, S.: Three-dimensional finite element modeling of laser cladding by powder injection: effects of powder feed rate and travel speed on the process, *Journal of Laser Applications*, 15, 2003, 153-160. <https://doi.org/10.2351/1.1585087>.
- [20] Urbanic, R.J.; Hedrick, R.W.: Saqib, S.; Nazemi, N.: Material bead deposition with 2 + 2 ½ multi-axis machining process planning strategies with virtual verification for extruded geometry, *International Journal of Advanced Manufacturing Technology*, 95(9-12), 2018, 3167-3184. <https://doi.org/10.1007/s00170-017-1376-9>.
- [21] Vectorization: <https://www.vectorization.org/>
- [22] Wood, G., Heat and Mass Transfer Aspects of Coaxial Laser Cladding and its Application to Nickel-Tungsten Carbide Alloys, PhD Dissertation, Department of Chemical and Materials Engineering, University of Alberta, 2017. [https://era.library.ualberta.ca/items/2476690e-fcb1-4bf2-8ff0-c96d3cf89843/view/608e8178-c1d1-4fa5-ba2a-190894178f18/Wood\\_Gentry\\_D\\_201704\\_PhD.pdf](https://era.library.ualberta.ca/items/2476690e-fcb1-4bf2-8ff0-c96d3cf89843/view/608e8178-c1d1-4fa5-ba2a-190894178f18/Wood_Gentry_D_201704_PhD.pdf)